communications materials

Article

https://doi.org/10.1038/s43246-024-00586-1

In-situ X-ray imaging of the breakup dynamics of current-carrying molten metal jets during arc discharge

Yuriko Sato [1] ✉, Takahisa Shobu[2], Aki Tominaga [3], Tomokazu Sano [1] & Yosuke Ogino [1] ✉

The flow dynamics of current-carrying molten metal jet breakup during arc discharge serves as mass and heat sources in wire-arc-based metal deposition processes, thereby optimizing the resultant product quality. However, the spatiotemporal flow interaction between the molten metal jet and the surrounding arc plasma remains unclear. Here, using in-situ synchrotron X-ray imaging, we simultaneously track surface deformation and internal flow in molten aluminum jets during argon arc discharge. We reveal that modulating the magnitude and path of the arc discharge current can accelerate the jet velocity by 200–300% beyond its initial injection speed, thereby facilitating significant jet elongation. Our results provide consistent evidence that the jet flow dynamics are predominantly governed by the interaction between the arc discharge current and its coaxial self-induced magnetic field. This study establishes a framework at the intersection of fluid dynamics and electromagnetism, contributing to optimized control and precision in wire-arc-based applications.

In the contemporary industrial framework, fusion welding and metal-based additive manufacturing stand as central technologies in both manufacturing and repair. These metallurgical processes facilitate the production of infrastructure, machinery, and everyday commodities. The performance of these processes is intrinsically linked to the precise utilization of appropriate mass sources (wire and powder) and heat sources (electric arcs, flames, lasers, and electron beams). The resultant efficiency, quality, durability, and esthetics of the final products are primarily derived from optimizing these sources[1–3].

Within gas metal arc welding[4] and arc-directed energy deposition[5–7], the mechanisms of melting, injection, and breakup of a molten metal jet serve as both mass and heat sources. This sequence, termed the metal transfer phenomenon[8], involves an electrode wire melting via arc and Joule heating, injecting a molten metal jet into the arc plasma, and subsequently breaking it up into droplets. These droplets are projected to a workpiece within just a few millimeters at rapid frequencies, approaching several hundred Hz, enabling accelerated deposition rates. Moreover, the metal transfer affects flow dynamics and solidification, governing the formation of the molten metal pool on a workpiece and the resulting mechanical properties[9,10]. This intricate relationship between physical processes and application presents a vital question: How can we decipher the metal transfer for a comprehensive scientific understanding and optimal industrial application?

The complexity of metal transfer arises from its nature as an electromagnetic fluid. The flow of this conductive fluid is driven by various forces like surface tension, electromagnetic (Lorentz) force, gravity, viscosity, and plasma drag force[8,11]. A critical competition occurs between surface tension and electromagnetic force, causing transitions of the breakup modes in metal transfer[12–14]. Increasing the arc discharge current amplifies the electromagnetic force due to the electromagnetic pinch effect[15,16], a concept established in fields like spacecraft propulsion[17] and nuclear fusion[18,19]. As this force modulates the internal flow of the molten metal jet and counteracts surface tension, the jet undergoes elongation, reminiscent of behaviors observed in Rayleigh jets[20–22]. Considering the spatial dynamics of jet deformation and its temporal interaction with arc plasma, current-carrying molten metal jets are subject to dynamic changes in electromagnetic force. Therefore, it becomes essential to visualize the temporal evolution of the internal flow within the spatially deforming jet.

While there is significant research on electromagnetic thermal fluid models to visualize the internal flow within the jet, their validations have often depended on monitoring the jet surfaces rather than direct internal examinations[23–25]. Despite numerous in-situ studies into the internal flow of molten metal pools through X-ray imaging[26–29] and heat-resistant glass windows[30–32], no study has yet directly revealed flow dynamics inside molten metal jets. This gap emerges from the necessity of non-contact velocimetry with high spatiotemporal resolution for molten metal. Conventional non-

[1]Graduate School of Engineering, Osaka University, Suita, Osaka, 565-0871, Japan. [2]Materials Sciences Research Center, Japan Atomic Energy Agency, Tokai, Ibaraki, 319-1195, Japan. [3]Materials Sciences Research Center, Japan Atomic Energy Agency, Sayo, Hyogo, 679-5148, Japan.
✉e-mail: sato@mapse.eng.osaka-u.ac.jp; ogino@mapse.eng.osaka-u.ac.jp

contact methods, such as particle image velocimetry[33,34] and laser Doppler velocimetry[34,35], are ineffective for opaque fluids. Additionally, applying Lorentz force velocimetry[36–38] to current-carrying fluid jets poses issues due to potential disturbances from external magnetic fields[39–41]. In light of these constraints, X-ray-based velocimetry stands out as a promising tool, uniquely suited to investigate opaque molten metal jets without perturbing their intrinsic flow dynamics.

In this study, synchrotron X-ray imaging is employed to visualize the flow dynamics inside a current-carrying molten metal jet during arc discharge. Through temporal particle tracking, we quantify the impact of current-related variables, such as the arc discharge current and the anode-cathode distance, on the internal flow within the jets. The X-ray particle tracking velocimetry demonstrates that the molten metal jets are electromagnetically accelerated beyond their initial injection flow due to the factors of current magnitude and path. These findings serve as a foundational step towards enhanced gas metal arc welding and arc-directed energy deposition.

Results

In-situ X-ray imaging techniques and methodological framework

In-situ X-ray imaging experiments were carried out at the beamline BL22XU in SPring-8[42]. An argon arc plasma was initiated between a continuously fed anode wire and twin tungsten cathode rods, thereby ensuring a symmetrical arc geometry along the longitudinal axis of the wire[43]. This arrangement in the arc discharge setup facilitated X-ray transmission into the wire fusion zone adjacent to the intense arc plasma, as detailed in Fig. 1a, Supplementary Note 1, and Supplementary Fig. 1. The experimental parameters, namely, the arc discharge current and anode-cathode distance, were meticulously adjusted. Notably, fine-tuning of the anode-cathode distance emerged as a critical factor in modulating the current path. As depicted in Fig. 1b, the discharge current flowed from the wire tip through the arc plasma, transitioning from a longitudinal direction to a radial path as it reached the tungsten cathodes. A minimized anode-cathode distance resulted in a significant spatial shift

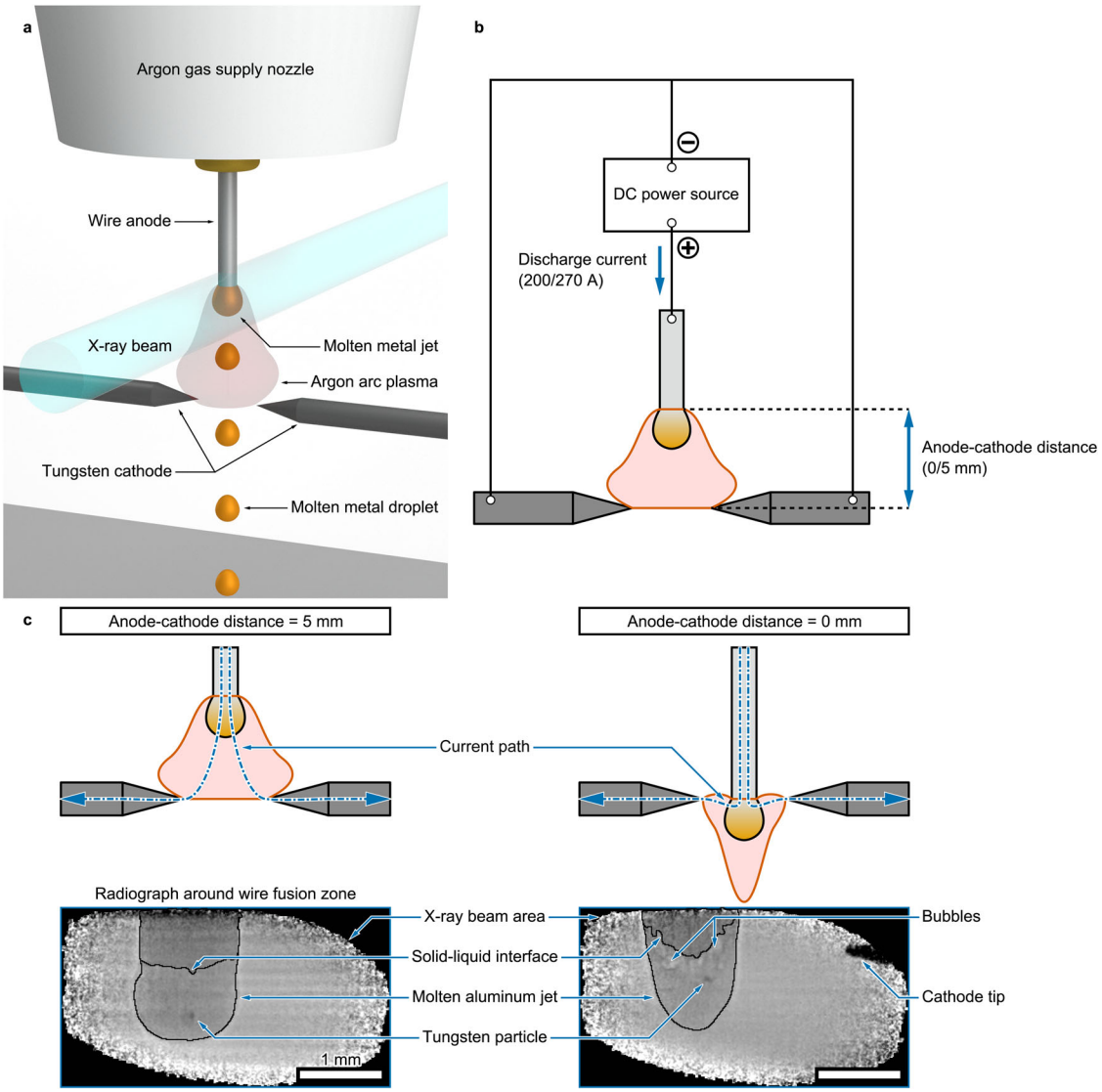

Fig. 1 | Experimental concept of synchrotron X-ray transmission imaging in wire-arc-based process. a Schematic illustrating the breakup of a current-carrying molten metal jet during arc discharge. The continuously fed wire formed a molten metal jet within the arc attachment site, where an X-ray beam with dimensions of 4.02 mm (width) × 2.19 mm (height) was transmitted through. **b** Schematic of the electrical circuit specific to the arc discharge setup with twin tungsten cathodes. The arc discharge current was directed from the aluminum anode wire to each of the two tungsten cathodes, with the discharge current and the anode-cathode distance serving as experimental parameters. **c** Representative radiographs capturing the injection of molten aluminum jets at a discharge current of 200 A and anode-cathode distances of 0 mm or 5 mm. The original images have dimensions of 448 pixels (width) × 296 pixels (height), captured with a pixel resolution of 86.25 pixels per mm and at a frame rate of 3 kHz. The radiographs shown in **c** are cropped to focus on the beam area. All scale bars = 1 mm.

of the current path from axial to radial direction, as evidenced in Fig. 1c. Radiographic snapshots were acquired at a 3 kHz frame rate utilizing a CsI scintillator-coupled, high-speed camera.

Our methodology involved utilizing pure tungsten particles, each with a maximum diameter of 53 μm, as tracers. These particles were instrumental in visualizing the internal flow dynamics within the molten metal jet through their spatiotemporal tracking. Positioned strategically along the coaxial center of the pure aluminum wire, the tracer particles were introduced longitudinally into the molten aluminum jet with the wire feed rate, subsequently following the flow of surrounding molten aluminum. The tungsten particles remained solid due to their higher melting point compared to aluminum, even until the detachment of the molten aluminum droplets. The difference in material properties resulted in distinct contrasts in the radiographs, differentiating the tracer particles and the molten aluminum jet (Fig. 1c). Although the incorporation of tracer particles introduced fine air bubbles near the solid-liquid interface, our comprehensive macroscopic assessments validated the robustness and reliability of our methodology, indicating consistent jet breakup periods and dimensions compared with tracer-free wires (Supplementary Note 2; Supplementary Fig. 2; Supplementary Movies 9, 10).

Time-dependent surface deformation during jet breakup cycles

Our investigation into the jet surface deformation encompassed four distinct conditions, manipulating the arc discharge current (200 and 270 A) and the anode-cathode distance (0 and 5 mm). Figure 2 depicts the sequential surface disturbances observed during the jet breakup cycles under these conditions (see details in Supplementary Movies 1–4). Except for the 270 A/0 mm setup, we observed consistent pinch-off within the observable beam areas (Fig. 2b, e, h), despite shorter breakup periods with the increased current and the minimized distance, from 6.3 down to 2.0 ms. In contrast, the 270 A/0 mm setup resulted in an axial jet elongation that exceeded the limitations of our imaging field, making the pinch-off unobservable (Fig. 2j–l).

Internal flow dynamics within molten metal jet

We analyzed internal flow dynamics by tracking the tracer particles, elucidating flow patterns influenced by jet deformation. During pinch-off, a tracer particle moved upward above the pinch-off location at 0.21 m s^{-1} and downward at 0.31 m s^{-1} below it, as shown in Fig. 3a, e (see Supplementary Movie 5). This bidirectional flow pattern was observed only under the 200 A/5 mm setup with the longest breakup period, while the other conditions primarily demonstrated a downward particle movement, as captured in Fig. 3b–d (see Supplementary Movies 6–8). To analyze the vertical propulsion of the molten metal jet and quantify its flow dynamics, independent of surface fluctuations, we introduced jet velocity as a specific parameter. This parameter represents the maximum velocity component in the z-direction, recorded by particles near the solid-liquid interface before the pinch-off process. Consistent with the breakup period findings, jet velocity increased with higher discharge current and shorter anode-cathode distance (Fig. 3f). Tracer particles, introduced into the jets at wire feed rates, experienced an increase in jet velocity of 200–300% relative to the wire feed rates. Specifically, under the 270 A/0 mm condition, we observed an average jet velocity of 0.64 m s^{-1}, representing a 3.1-fold increase over the wire feed rate of 0.205 m s^{-1}.

Discussion

Our study marks the successful in-situ visualization and quantification of current-carrying molten metal jet acceleration within an arc discharge, achieved through synchrotron X-ray transmission imaging. We identified that jet velocity is directly influenced by both the magnitude and path of the arc discharge current. These insights offer substantial strategies for fine-tuning essential parameters, such as discharge currents and anode-cathode distances, in wire-arc-based metal deposition processes. Moreover, our work contributes vital data on aluminum, a material with wide-ranging industrial applications.

Arc discharge current is intrinsically linked to electromagnetic force, which governs electromagnetic fluid flow. Previous computational models have established that both the magnitude and the path of the discharge current play critical roles in amplifying electromagnetic force and consequently affecting fluid flow[44–49]. Focusing first on the magnitude of discharge current, Choi et al. revealed that increased current intensifies the axial flow, serving as the primary driving factor for droplet detachment[44,45]. Despite using different wire materials and diameters, our measurements closely align with theirs, both in terms of the observed trends and the specific velocity ranges reported. Specifically, they reported calculated maximum velocities of 0.43 m s^{-1} and 1.7 m s^{-1} at currents of 150 A and 300 A for a 1.6-mm-diameter steel wire, respectively. Turning to the aspect of the discharge current path, Ogino et al. pointed out the role of the current path in jet tapering or elongation: a radially expanding current path intensifies the radial electromagnetic force near the solid-liquid interface rather than at the bottom of the jets[46,47]. As with our observations when changing conditions from 270 A/5 mm to 270 A/0 mm, their computational results demonstrated jet elongation when the current path spread out and promoted current leakage into the arc plasma from the side rather than the bottom of molten mild steel jets. However, their qualitative discussion was limited to the radial electromagnetic force pinching the jet, without addressing the quantitative response of the axial flow induced by this force.

Interestingly, comparable acceleration mechanisms are observed in plasma jet phenomena, driven by the interaction between direct current and its coaxial self-induced magnetic field. This cross-disciplinary evidence provides a broader perspective to our study. According to the Maecker formula[17], a well-established theory in plasma jet studies, this acceleration mechanism is achieved through two distinct effects: the blowing effect by axial electromagnetic force, and the pumping effect by induced axial pressure force known as the electromagnetic pinch effect[17,50,51]. Total jet thrust is governed by both the magnitude of discharge current and the extent of current path expansion. For example, studies on plasma jet applications, including tungsten inert gas welding[4], consistently provide both theoretical and experimental evidence that plasma jet velocities increase with the discharge current[8,17,52–54]. This relationship stems from the conversion of electromagnetic energy into kinetic energy. Furthermore, magnetoplasmadynamic thrusters, expected for future aerospace applications, exhibit increased total thrust with the anode-cathode radius ratio—a key metric of discharge current path expansion[17,55]. While plasma jets are governed by single-phase electromagnetic fluid flow, the metal transfer phenomena involve more intricate multi-phase flows. These complexities mean that the distribution of electrical current between the arc plasma and the molten metal jet is subject to material-specific variables, such as electrical conductivity. Previous studies have identified that the current level influencing jet breakup modes depends on the material properties of both the wire and the arc plasma[47,56–60]. However, given that both plasma jet and metal transfer are driven by the electromagnetic interaction between current and its self-induced magnetic field, the cross-disciplinary insights from single-phase flow in plasma jet can still help to clarify the effective impact of current distribution on multi-phase flows in metal transfer.

For wire material, aluminum was selected not only due to its widespread industrial use in wire-arc-based processes but also to address specific technical challenges associated with synchrotron X-ray transmission imaging. As a light metal, aluminum provides a distinct contrast in radiographs compared to heavier metals like tungsten, enhancing the visibility of tracers during particle tracking analysis. Although based on this technical selection, our aluminum-based findings, which show internal flow acceleration within elongated jets as evidenced by increased jet velocities, offer insights that could potentially extend to other materials. Sato et al. revealed that the fundamental electromagnetic mechanisms driving jet breakup remained consistent across various wire materials such as aluminum, copper, iron, nickel, and titanium. While the threshold current required for jet elongation varied with the electrical conductivity of each material, all tested materials experienced jet elongation through either an increased magnitude of current or an expansion of the current path. Building on the surface observations by Sato et al., our study

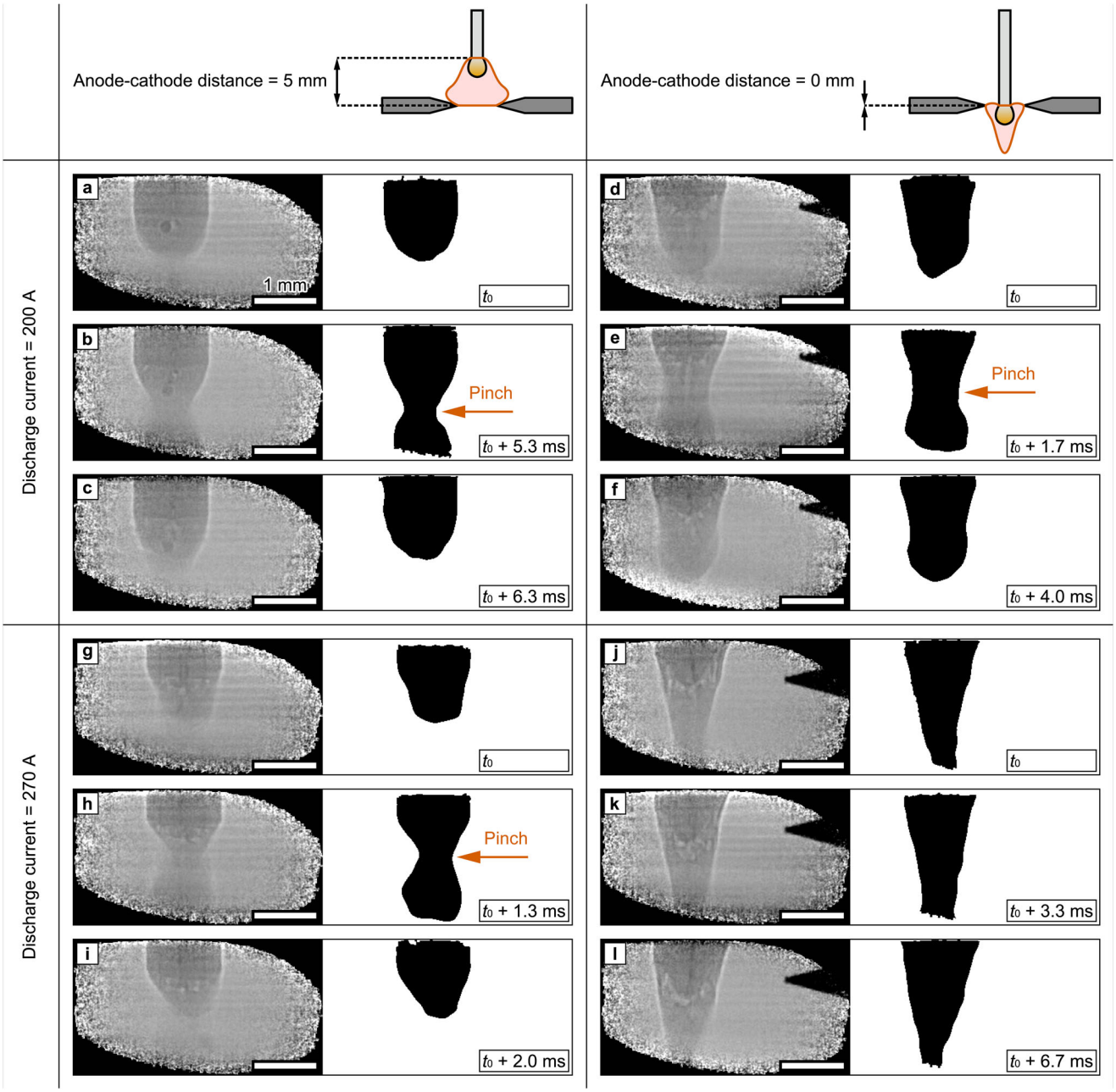

Fig. 2 | Time-series analysis of surface dynamics during molten aluminum jet breakup. Time-series images for the four conditions of arc discharge current and anode-cathode distance: **a–c** 200 A/5 mm (Supplementary Movie 1), **d–f** 200 A/0 mm (Supplementary Movie 2), **g–i** 270 A/5 mm (Supplementary Movie 3), and (**j–l**) 270 A/0 mm (Supplementary Movie 4). Each image features a radiograph on the left and its corresponding boundary-extracted image of the jet surface on the right. t_0 represents the time elapsed from the start of recording to the initiation of surface tracking. Single breakup cycles are presented for the conditions of 200 A/5 mm, 200 A/0 mm, and 270 A/5 mm. Pinch-off is observed within the beam area for all conditions except the 270 A/0 mm condition (**b, e**, **h**). All scale bars = 1 mm.

extends their findings through the internal flow observations within molten aluminum jets and thereby emphasizes the interconnected nature of electromagnetism and fluid dynamics. Indeed, there is still a clear need for additional experiments to accurately measure velocities in wire materials beyond aluminum. Nevertheless, our findings suggest the potential generalization that electromagnetic force, by driving internal flow acceleration, can induce jet elongation across a diverse range of wire materials.

For gas composition, pure argon was selected to shield the molten aluminum jets and tungsten cathodes from oxidation. However, in practical wire-arc-based processes, a variety of gases, including helium, carbon dioxide, and mixtures of argon with other gases, are commonly used to control the power density of the arc plasma heat source and the resulting material deposition characteristics. While wire selection affects material deposition characteristics primarily through its material properties, gas selection influences these characteristics through a combination of material properties and geometric factors. Firstly, as with the wire, the material properties of the arc plasma, particularly its electrical conductivity, are crucial in determining jet breakup characteristics. Ogino et al. conducted numerical simulations to examine the effect of electrical conductivity of arc plasma by altering the mixing ratio of argon and carbon dioxide gases[47]. They revealed that the electrical conductivity distribution from the side to the bottom of the molten metal jet determines the current path and consequently the jet breakup behavior. Secondly, the constriction of the arc plasma itself is a geometric factor that governs the arc attachment to the molten metal jet and confines the current path. For example, with helium or carbon dioxide, the arc plasma constricts significantly compared to argon-

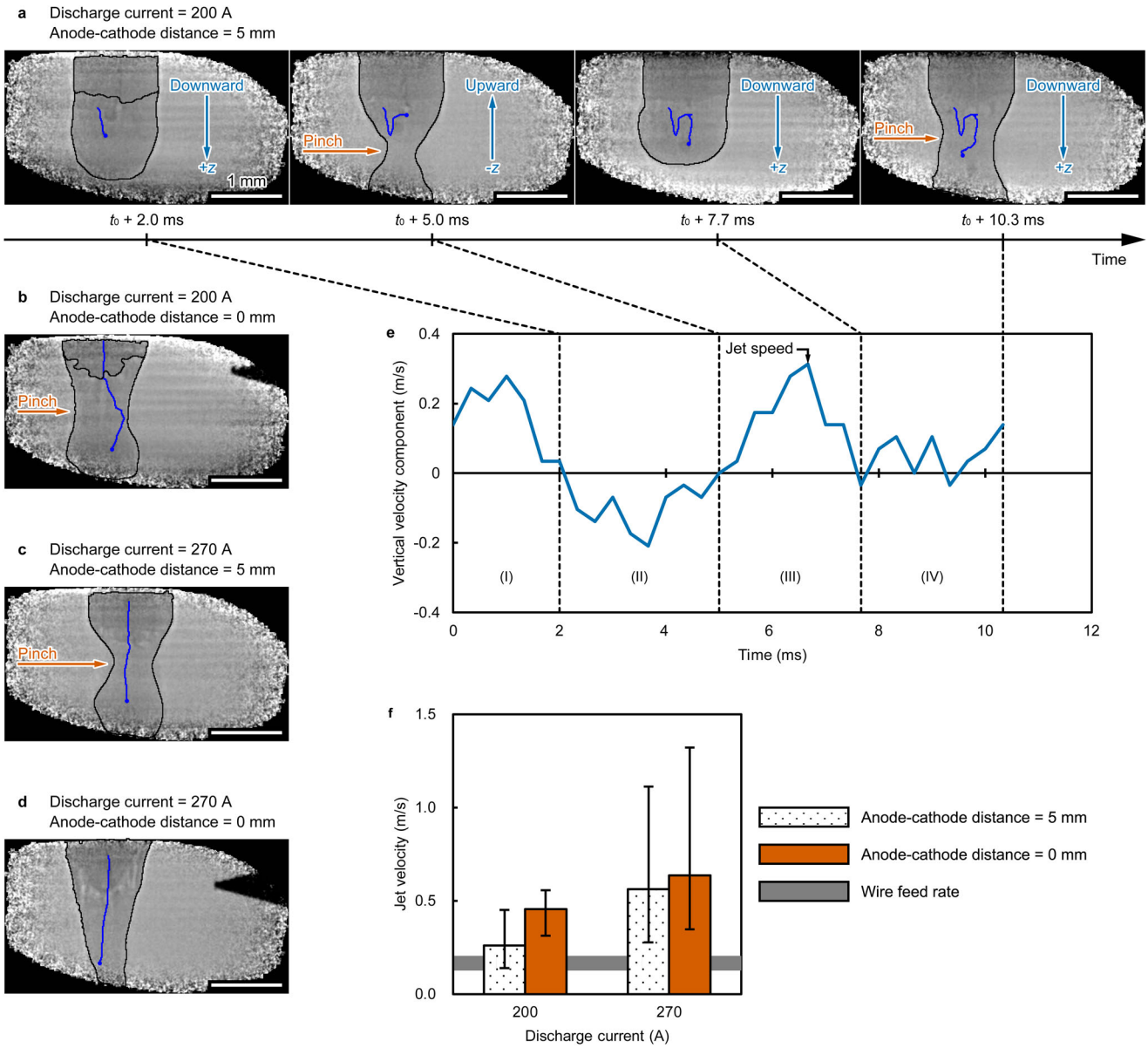

Fig. 3 | Quantification of molten aluminum jet flow dynamics using particle tracking analysis. Radiographs with tracer particle trajectories under the four conditions: **a** 200 A/5 mm (Supplementary Movie 5), **b** 200 A/0 mm (Supplementary Movie 6), **c** 270 A/5 mm (Supplementary Movie 7), and **d** 270 A/0 mm (Supplementary Movie 8). In these images (**a**–**d**), black lines indicate the jet surface or the solid-liquid interface, while blue lines with rounded endpoints represent the particle trajectories; the rounded endpoints mark the end of particle tracking. **e** Time-course graph depicting the vertical component of particle velocity for the 200 A/5 mm condition. The horizontal axis represents the time elapsed since the start of particle tracking, with the initial frame set as the time reference ($t = t_0$). The graph divides into four phases, each corresponding to a distinct stage of pinch-off in **a**: (I) particle descent within the pre-pinch rounded jet at $t_0 + 2.0$ ms, (II) ascent of the particle located above the pinch-off at $t_0 + 5.0$ ms, (III) particle descent with another pre-pinch rounded jet at $t_0 + 7.7$ ms, and (IV) continued descent of the particle located below the pinch-off at $t_0 + 10.3$ ms. **f** Bar graph quantifying the jet velocities across the four conditions. Jet velocity refers to the maximum vertical component of particle velocity observed near the solid-liquid interface before pinch-off. Bars with a white background and black dot pattern indicate an anode-cathode distance of 5 mm, while bars filled with red indicate an anode-cathode distance of 0 mm. In the bar graph, error bars represent the range between the maximum and minimum jet velocities for each condition. As the discharge current increased and the anode-cathode distance decreased, the jet velocity increased. Under all tested conditions, the jet velocities exceed the wire feed rate by 200% to 300%, represented in the gray area. All scale bars = 1 mm.

rich gases, leading to a bulged jet instead of an elongated one[56]. In our experiment, increasing the anode-cathode distance corresponds to the effect of arc constriction. The observed suppression of jet elongation under conditions from 270 A/0 mm to 270 A/5 mm is comparable to the suppression seen when changing the shielding gas composition from argon-rich gases to helium or carbon dioxide. Incorporating both factors, even at the same current level, the resultant current path is determined by the spatial distribution of arc electrical conductivity and the geometric constraints imposed by arc constriction. Additionally, the spatiotemporal mixing of arc plasma from the shielding gas and metal vapor from the overheated jet causes intricate fluctuations in arc plasma characteristics. Therefore, detailed plasma measurements and numerical simulations are essential for gaining a clearer understanding of the interaction between the arc plasma and the molten metal jet.

Despite our primary focus on electromagnetic force and surface tension, it remains essential to also consider the potential contributions of other driving forces such as shear stress and gravity. Specifically, shear stress includes plasma drag force and the Marangoni effect. During arc discharge,

these forces are generated at the molten metal surface and diffuse inward. Plasma drag force acts as a directional force, aligning with the jet injection direction, but becomes less dominant in high-current regions where droplet size decreases, similar to the gravitational effect[61]. In contrast, the Marangoni effect is driven by temperature-dependent gradients in surface tension and acts as a counteractive force against the downflow of molten metal jets, especially in materials without surface-active elements. This effect is further intensified by three factors[62]: greater temperature difference in high power density welding processes like laser welding; lower thermal diffusivity in materials such as steel; and larger spatial scale of the flow as observed in molten metal pools. The downflow observed in the jet core suggests that, at least in this region, the Marangoni effect has a limited counteractive influence on the velocity profile under the tested conditions. Such limitations are likely due to spatial flow scale rather than temperature difference. Although a greater temperature difference might be locally expected for droplets compared to pools, due to the rapid phase transition of the wire from solid to liquid and gas, this effect is counteracted by the small spatial scale. Additionally, the small spatial flow scale significantly amplifies the electromagnetic effect on droplets compared to pools, as it is proportional to the square of the current density. Consequently, the electromagnetic effect can be more substantial than the Marangoni effect. However, given the complexity of surface interactions in a free surface flow, the potential impact of shear stress on jet breakup dynamics still remains to be elucidated. To fully understand these effects, it would be beneficial to improve visualization coverage by dispersing tracer particles throughout the entire jet, including near the surface, rather than focusing solely on the jet core as in this study.

The reliability of our flow visualization relies on the sufficient ability of tracer particles to respond to molten metal flow. As a possible cause of tracer particles deviating from the molten metal flow, one might consider the potential for gravity to accelerate tungsten particles. However, even when accounting for their higher density relative to the surrounding molten aluminum, the influence of gravity proves negligible. Specifically, we applied Stokes' law within a moving coordinate system descending at the wire feed rate, i.e., the rate at which both tracer particles and molten aluminum are introduced into the jet. The terminal settling velocity for a sphere particle in free-fall is calculated as $v = (\rho_p - \rho_f)gD^2/18\mu$[63], where ρ_p and ρ_f represent the particle and fluid densities, g is the gravitational acceleration, D is the particle diameter, and μ is the fluid viscosity. For pure tungsten particles with a diameter of 53 μm[64], the calculated settling velocity is a mere 0.02 m s^{-1}. This figure is significantly lower than the velocity increments when we measured against the wire feed rate, validating the negligible role of gravity in our experiment. Furthermore, calculating the Stokes number $\mathrm{St} = \rho_p D^2 U/18\mu L$ results in $\mathrm{St} \approx 10^0$, with a representative velocity U of 1 m s^{-1} and a characteristic length L of 1.2 mm. This estimation confirms that the selected particle size is suitable to ensure both the necessary radiograph contrast and the sufficient ability to closely follow the flow. However, it should be noted that there is still room for improvement in the selection of tracer particles, particularly regarding shape and size distribution. Our experiments used mechanically milled tungsten powder, which included some particles with low circularity and others much smaller than the pixel size. These fine particles needed to cluster to be observed due to the weak X-ray attenuation effect, which merely degraded the radiograph contrast between the tracer particles and the molten aluminum. To enhance the quality of flow visualization, it would be beneficial to use atomized 10-μm-scale powder with high circularity and a narrow size distribution. Additionally, the method of introducing tracer particles to the wire should be optimized to avoid air bubble formation, which can obstruct the particle movement.

Two technical challenges in our velocimetry may have introduced errors, resulting in discrepancies between the measured and actual velocities: the inability to track three-dimensional particle movements and the restricted imaging area that was unable to cover the entire jet. Firstly, despite the inherently three-dimensional trajectories of the particles, our velocimetry could only capture their projections onto the two-dimensional plane perpendicular to the X-ray beam (the xz-plane). This limitation might have led to an underestimation of speeds if the transverse tracer movement in the y-direction was significant, as a brief estimation is provided in Supplementary Note 3 and Supplementary Fig. 3. Nevertheless, the primary focus of this study is the axial elongation of molten metal jets in the z-direction. Since the vertical component is likely the most critical for axial elongation, evaluating only the z-component as the jet velocity helps minimize potential inaccuracies due to particle movement in other directions. This approach allows us to effectively assess the contribution of internal flow dynamics to jet elongation, within the constraints of our velocimetry. Secondly, under the condition of 270 A/0 mm, the molten aluminum jet elongated beyond our imaging capability, making the complete pinch-off unobservable. A larger imaging area could potentially capture faster velocities in the lower segments of the elongated jet. Lastly, future work could offer a comprehensive dataset for flow and driving force distribution, thereby enhancing the comparability of experimental and numerical findings.

In summary, our research has elucidated the core mechanisms governing the acceleration of current-carrying molten metal jets during arc discharge, thereby clarifying key factors for advancing wire-arc-based applications. This deeper understanding establishes a robust framework for enhancing both the quality and efficiency of wire-arc-based technologies, including gas metal arc welding and arc-directed energy deposition. Additionally, our work contributes to interdisciplinary knowledge at the intersection of fluid dynamics and electromagnetism. Applying the X-ray imaging technique, we identified that the arc discharge current and its distribution significantly influence the electromagnetic force and flow dynamics within the molten metal jet. These lead to a jet velocity several times faster than the wire feed rate, subsequently affecting the jet breakup period and deformation patterns. Our foundational understanding of the interplay between molten metal and arc plasma offers a viable groundwork for the optimization of wire-arc-based processes, providing valuable insights for future studies on electromagnetic thermal fluid dynamics.

Methods

Materials and experimental design

We initiated an argon arc discharge between a continuously fed aluminum wire and two tungsten rods (see details in Supplementary Note 1 and Supplementary Fig. 1)[43]. In our experimental setup, the arc discharge current oriented from the wire tip, flowed through the arc plasma, and transitioned from a longitudinal to a radial direction as it reached the tungsten cathodes. For the consumable anode, we employed commercially pure aluminum alloy (A1070) wire with a diameter of 1.2 mm and a length of 500 mm. The detailed chemical composition of the A1070 wire is provided in Supplementary Table 1. This wire contained a coaxial hole of 0.1 mm in diameter, which was filled with a mixture of atomized 3-μm aluminum powder and tungsten powder up to a size of 53 μm at a mass ratio of 9 to 1. The wire feed rate was controlled using a single-axis slider and varied from 0.126 to 0.205 m s^{-1}, based on the discharge current set by a constant-current power source (Welbee Inverter T500P, DAIHEN). In contrast, the non-consumable cathodes consisted of 1.6-mm-diameter tungsten rods, doped with 2 wt.% La_2O_3 and featuring a 30-degree tip angle. To ensure stable cathode spots and minimize arc plasma fluctuations, the tungsten rods were inserted 10 mm below the contact tip throughout the experiments. These rods were oriented symmetrically along the longitudinal axis of the anode wire with a 4 mm gap. Pure argon gas was supplied at a rate of 20 L/min through a coaxial nozzle aligned with the anode wire. Experimental variables included the arc discharge current (either 200 or 270 A) and the anode-cathode distance, measured as the height from the solid-liquid interface of the anode wire to the tips of the tungsten cathodes (either 0 or 5 mm). To enhance the reliability of the experiments, each experimental condition was repeated at least three times.

Synchrotron X-ray transmission imaging

Our experiments were carried out at the beamline BL22XU in SPring-8, Japan[42]. Incident X-rays generated from a planar undulator were monochromatized by a Si(111) double-crystal monochromator and 30 keV X-rays were used in our experiments. The beam dimensions of 4.02 mm

(width) × 2.19 mm (height) were measured specifically where the beam transmitted through the fusion zone of the anode wire. The detection system employed a high-speed camera manufactured by NAC Image Technology Inc. that was lens-coupled to a CsI scintillator. Operating at frame rates of 3 kHz, the camera captured images with dimensions of 448 pixels (width) × 296 pixels (height), corresponding to a pixel resolution of 86.25 pixels per mm.

Image analysis and quantification

Image processing was conducted using Fiji software[65]. The first step involved background noise minimization through a background removal algorithm defined by the equation $I_1 = (I_0 - I_{dark})/(I_{back} - I_{dark})$. In this formula, I_1 refers to the processed image intensity; I_0 represents the raw image intensity; I_{back} denotes the mean intensity of 100 background images; I_{dark} is the mean intensity of 100 dark-field images. In the resulting radiographs, different materials could be distinguishable based on their intensities: tungsten particles appeared as darker regions, molten aluminum as medium intensity, and the surrounding gas as a light area. This distinct contrast was attributable to the different X-ray attenuation effects for each material. For the kinematic analysis of tungsten particles within the molten aluminum jet, we employed the Manual Tracking plugin, developed by Fabrice P. Cordelières at Institut Curie, Orsay, France. This plugin provided detailed data, including pixel coordinates, velocity, inter-frame displacement, and pixel intensity. To accurately quantify jet flow dynamics while eliminating the effects of surface deformation, the tracking was confined to particles located near the solid-liquid interface. To ensure reproducibility, the analysis utilized data exclusively from the quasi-steady period, with the arc ignition and extinction periods excluded. The jet velocity for each condition was evaluated by calculating the average from at least nine particle tracking trajectories. Our image analysis can introduce a potential velocity error of approximately 0.08 m s^{-1} (see Supplementary Note 4 and Supplementary Table 2 for further information).

Data availability

The radiograph data supporting the findings of this study are available within the paper and its supplementary movies. Other datasets generated and analyzed during this study are not publicly available due to their extensive size. However, the data are available from the corresponding author Y. O. on reasonable request.

Received: 27 January 2024; Accepted: 22 July 2024;
Published online: 20 August 2024

References

1. Cooke, S., Ahmadi, K., Willerth, S. & Herring, R. Metal additive manufacturing: Technology, metallurgy and modelling. *J. Manuf. Process.* **57**, 978–1003 (2020).
2. Lewandowski, J. J. & Seifi, M. Metal additive manufacturing: A review of mechanical properties. *Annu. Rev. Mater. Res.* **46**, 151–186 (2016).
3. Liu, Z. et al. Additive manufacturing of metals: microstructure evolution and multistage control. *J. Mater. Sci. Technol.* **100**, 224–236 (2022).
4. Murphy, A. B. A perspective on arc welding research: the importance of the arc, unresolved questions and future directions. *Plasma Chem. Plasma Process.* **35**, 471–489 (2015).
5. Williams, S. W. et al. Wire + arc additive manufacturing. *Mater. Sci. Technol.* **32**, 641–647 (2016).
6. Xia, C. et al. A review on wire arc additive manufacturing: monitoring, control and a framework of automated system. *J. Manuf. Syst.* **57**, 31–45 (2020).
7. Pattanayak, S. & Sahoo, S. K. Gas metal arc welding based additive manufacturing—a review. *CIRP J. Manuf. Sci. Technol.* **33**, 398–442 (2021).
8. Lancaster, J. F. *The Physics of Welding*. (Pergamon Press, Oxford, 1986).
9. Mukherjee, M. & Pal, T. K. Influence of mode of metal transfer on microstructure and mechanical properties of gas metal arc-welded modified ferritic stainless steel. *Metall. Mater. Trans. A* **43**, 1791–1808 (2012).
10. Aldalur, E., Suárez, A. & Veiga, F. Metal transfer modes for wire arc additive manufacturing Al-Mg alloys: influence of heat input in microstructure and porosity. *J. Mater. Process. Technol.* **297**, 117271 (2021).
11. Greene, W. J. An analysis of transfer in gas-shielded welding arcs. *Trans. AIEE, Part II: Appl. Ind.* **79**, 194–203 (1960).
12. Ruckdeschel, W. E. W. Classification of metal transfer. in *International Institute of Welding Documents* IIW Doc. XII-636-76 (1976).
13. Scotti, A., Vladimir, P. & Lucas, W. A scientific application oriented classification for metal transfer modes in GMA welding. *J. Mater. Process. Technol.* **212**, 1406–1413 (2012).
14. Ogino, Y. & Hirata, Y. Numerical simulation of metal transfer in argon gas-shielded GMAW. *Weld. World* **59**, 465–473 (2015).
15. Northrup, E. F. Some newly observed manifestations of forces in the interior of an electric conductor. *Phys. Rev. (Ser. I)* **24**, 474–497 (1907).
16. Murty, G. S. Instability of a conducting fluid cylinder in the presence of an axial current, a longitudinal magnetic field and a coaxial conducting cylinder. *Ark. Fys.* **19**, 483–497 (1961).
17. Maecker, H. Plasmaströmungen in lichtbögen infolge eigenmagnetischer kompression. *Z. Phys.* **141**, 198–216 (1955).
18. Haines, M. G. A review of the dense Z-pinch. *Plasma Phys. Control. Fusion* **53**, 093001 (2011).
19. Spielman, R. B. & de Groot, J. S. Z pinches—A historical view. *Laser Part. Beams* **19**, 509–525 (2001).
20. Eggers, J. Nonlinear dynamics and breakup of free-surface flows. *Rev. Mod. Phys.* **69**, 865–929 (1997).
21. Leib, S. J. & Goldstein, M. E. The generation of capillary instabilities on a liquid jet. *J. Fluid Mech.* **168**, 479–500 (1986).
22. Clanet, C. & Lasheras, J. C. Transition from dripping to jetting. *J. Fluid Mech.* **383**, 307–326 (1999).
23. Ikram, A. & Chung, H. Numerical simulation of arc, metal transfer and its impingement on weld pool in variable polarity gas metal arc welding. *J. Manuf. Process.* **64**, 1529–1543 (2021).
24. Komen, H., Shigeta, M. & Tanaka, M. Numerical simulation of molten metal droplet behavior in gas metal arc welding by three-dimensional incompressible smoothed particle hydrodynamics method. *J. Flow. Control Meas. Vis.* **6**, 66–81 (2018).
25. Zhao, Y. & Chung, H. Numerical simulation of droplet transfer behavior in variable polarity gas metal arc welding. *Int. J. Heat. Mass Transf.* **111**, 1129–1141 (2017).
26. Aucott, L. et al. Revealing internal flow behaviour in arc welding and additive manufacturing of metals. *Nat. Commun.* **9**, 5414 (2018).
27. Wu, F. et al. Time evolved force domination in arc weld pools. *Mater. Des.* **190**, 108534 (2020).
28. Zhang, X. et al. Progress in in situ x-ray imaging of welding process. *Rev. Sci. Instrum.* **93**, 071501 (2022).
29. Zhang, X. et al. Key mechanism of metal transfer and characteristic of cavity evolution during SAW using in-situ X-ray imaging method. *J. Mater. Process. Technol.* **319**, 118057 (2023).
30. Wang, L., Liu, Y., Li, Y., Zhu, M. & Qiao, J. Study on mechanism of the effect of Al element on the arc shape and molten pool fluctuation pattern in flux bands constricting arc welding (FBCA). *J. Manuf. Process.* **101**, 882–891 (2023).
31. Li, S., Chen, G., Zhang, M., Zhou, Y. & Zhang, Y. Dynamic keyhole profile during high-power deep-penetration laser welding. *J. Mater. Process. Technol.* **214**, 565–570 (2014).
32. Zhang, M. J., Chen, G. Y., Zhou, Y., Li, S. C. & Deng, H. Observation of spatter formation mechanisms in high-power fiber laser welding of thick plate. *Appl. Surf. Sci.* **280**, 868–875 (2013).
33. Raffel, M., Willert, C. E., Wereley, S. T. & Kompenhans, J. *Particle Image Velocimetry: A Practical Guide*. (Springer International Publishing, Cham, 2018).

34. Adrian, R. J. Particle-imaging techniques for experimental fluid mechanics. *Annu. Rev. Fluid Mech.* **23**, 261–304 (1991).
35. Foreman, J. W. Jr, George, E. W. & Lewis, R. D. Measurement of localized flow velocities in gases with a laser doppler flowmeter. *Appl. Phys. Lett.* **7**, 77–78 (1965).
36. Thess, A., Votyakov, E. V. & Kolesnikov, Y. Lorentz force velocimetry. *Phys. Rev. Lett.* **96**, 164501 (2006).
37. Thess, A., Votyakov, E., Knaepen, B. & Zikanov, O. Theory of the Lorentz force flowmeter. *N. J. Phys.* **9**, 299 (2007).
38. Thess, A., Kolesnikov, Y. & Karcher, C. Method and arrangement for the contactless inspection of moving electrically conductive substances. Patent No. WO 2007/033982 A1 (2007).
39. Wu, H., Chang, Y., Lu, L. & Bai, J. Review on magnetically controlled arc welding process. *Int. J. Adv. Manuf. Technol.* **91**, 4263–4273 (2017).
40. Sun, Q. et al. Arc characteristics and droplet transfer process in CMT welding with a magnetic field. *J. Manuf. Process.* **32**, 48–56 (2018).
41. Wang, L., Chen, J., Wu, C. & Luan, S. Numerical analysis of arc and droplet behaviors in gas metal arc welding with external compound magnetic field. *J. Mater. Process. Technol.* **282**, 116638 (2020).
42. Shobu, T. et al. Wide band energy beamline using Si (111) crystal monochromators at BL22XU in SPring-8. *AIP Conf. Proc.* **879**, 902–906 (2007).
43. Sato, Y., Ogino, Y. & Sano, T. Process parameters and their effect on metal transfer in gas metal arc welding: a driving forces perspective. *Weld. World* **68**, 905–913 (2024).
44. Choi, S. K., Yoo, C. D. & Kim, Y.-S. Dynamic simulation of metal transfer in GMAW, part 1: Globular and spray transfer modes. *Weld. J.* **77**, 38–44 (1998).
45. Choi, S. K., Yoo, C. D. & Kim, Y.-S. The dynamic analysis of metal transfer in pulsed current gas metal arc welding. *J. Phys. D: Appl. Phys.* **31**, 207–215 (1998).
46. Ogino, Y., Hirata, Y., Kihana, S. & Nitta, N. Numerical simulation of free-flight transfer by a 3D metal transfer model. *Q. J. Jpn. Weld. Soc.* **36**, 94–103 (2018).
47. Ogino, Y., Hirata, Y. & Asai, S. Discussion of the effect of shielding gas and conductivity of vapor core on metal transfer phenomena in gas metal arc welding by numerical simulation. *Plasma Chem. Plasma Process.* **40**, 1109–1126 (2020).
48. Zhao, Y. & Chung, H. Numerical simulation of the transition of metal transfer from globular to spray mode in gas metal arc welding using phase field method. *J. Mater. Process. Technol.* **251**, 251–261 (2018).
49. Tanaka, M. et al. Effect of shielding gas composition on gas metal arc welding phenomena using rare earth metal added wire. *Q. J. Jpn. Weld. Soc.* **38**, 438–447 (2021).
50. Jahn, R. G. *Physics of Electric Propulsion*. (McGraw Hill Book, 1968).
51. Myers, R., Lapointe, M. & Mantenieks, M. MPD thruster technology. in *Conference on Advanced Space Exploration Initiative Technologies* https://doi.org/10.2514/6.1991-3568 (1991).
52. Squire, H. B. The round laminar jet. *Q. J. Mech. Appl. Math.* **4**, 321–329 (1951).
53. Adonyi, Y., Richardson, R. & Baeslack, W. Investigation of arc force effects in subsurface GTA welding. *Weld. J.* **71**, 321–330 (1992).
54. Planche, M. P., Coudert, J. F. & Fauchais, P. Velocity measurements for arc jets produced by a DC plasma spray torch. *Plasma Chem. Plasma Process.* **18**, 263–283 (1998).
55. Kawasaki, A., Kubota, K., Funaki, I. & Okuno, Y. MHD simulation and thermal design of an MPD thruster. *Trans. Jpn. Soc. Aeronaut. Space Sci.* **12**, Pb_19–Pb_25 (2014).
56. Rhee, S. & Kannatey-Asibu, E. Observation of metal transfer during gas metal arc welding. *Weld. J.* **71**, 381–386 (1992).
57. Cooksey, C. J. & Milner, D. R. Metal transfer in gas-shielded arc welding. in *Physics of the welding arc: A symposium organized by the Institute of Welding* 123–132 (1962).
58. Kim, Y.-S. & Eager, T. W. Analysis of metal transfer in gas metal arc welding. *Weld. J.* **72**, 269–278 (1993).
59. Ogino, Y., Hirata, Y. & Murphy, A. B. Numerical simulation of GMAW process using Ar and an Ar–CO2 gas mixture. *Weld. World* **60**, 345–353 (2016).
60. Sato, Y., Ogino, Y. & Sano, T. Role of material properties on metal transfer dynamics in gas metal arc welding. *J. Mater. Process. Technol.* **326**, 118347 (2024).
61. Li, K., Wu, Z. & Liu, C. Measurement and calculation of plasma drag force in arc welding based on high-speed photography technology and particle dynamics. *Mater. Des.* **85**, 97–101 (2015).
62. Limmaneevichitr, C. & Kou, S. Experiments to simulate effect of Marangoni convection on weld pool shape. *Weld. J.* **79**, 231–237 (2000).
63. Lamb, H. *Hydrodynamics*. (Cambridge Univ. Press, 1895).
64. Smithells, C. J. *Smithells Metals Reference Book*. (Butterworth-Heinemann, 1976).
65. Schindelin, J. et al. Fiji: an open-source platform for biological-image analysis. *Nat. Methods* **9**, 676–682 (2012).

Acknowledgements

Y. O. acknowledge funding from the Advanced Research Infrastructure for Materials and Nanotechnology in Japan (ARIM Japan) of the Ministry of Education, Culture, Sports, Science and Technology (MEXT), Japan (Grant No. JPMXP1222AE0008) and the Shared-Use Program of JAEA Facilities (Proposal No. 2022A-E08). Y. S. acknowledge funding from the Grant-in-Aid for JSPS Fellows of the Japan Society for the Promotion of Science (JSPS), Japan (Grant No. JP22KJ2184). The synchrotron radiation experiments were performed at SPring-8 beamline BL22XU with the approval of the Japan Synchrotron Radiation Research Institute (JASRI) (Proposal No. 2022A3739). We also thank S. Nakajima, H. Ohgushi, I. Hirota, and T. Maruyama for their assistance in this beamtime.

Author contributions

Y. S. and Y. O. conceived the idea and designed the experiments (arc discharge setup). Y. S. and Y. O. performed the experiments. T. Sh. and A. T. designed and supervised the experiments (beamline and imaging). Y. S. analyzed the data and drafted the original manuscript. Y. O. supervised the data analysis and secured the funding support. T. Sh. assisted in the data analysis (image processing). Y. O. and T. Sh. reviewed and revised the manuscript. Y. O. and T. Sa. supervised the entire project.

Competing interests

The authors declare no competing interests.

Additional information

Supplementary information The online version contains supplementary material available at https://doi.org/10.1038/s43246-024-00586-1.

Correspondence and requests for materials should be addressed to Yuriko Sato or Yosuke Ogino.

Peer review information *Communications Materials* thanks the anonymous reviewers for their contribution to the peer review of this work. Primary Handling Editors: Cang Zhao and John Plummer. A peer review file is available.